




**COMMUNICATION**

Mechanotransduction by Membrane Proteins

# Characterizing the lipid fingerprint of the mechanosensitive channel Piezo2

 Yiechang Lin<sup>1</sup> , Amanda Buyan<sup>1</sup> , and Ben Corry<sup>1</sup> 

**Piezo2 is a mechanosensitive ion channel that plays critical roles in sensing touch and pain, proprioception, and regulation of heart rate. Global knockout of Piezo2 leads to perinatal lethality in mice, and Piezo2 gain-of-function mutations are associated with distal arthrogryposis, a disease characterized by congenital joint contractures. Emerging evidence suggests that Piezo channels (Piezo1 and Piezo2) can be regulated by their local membrane environment and particularly by cholesterol and phosphoinositides. To characterize the local Piezo2 lipid environment and investigate key lipid–protein interactions, we carried out coarse-grained molecular dynamics simulations of Piezo2 embedded in a complex mammalian membrane containing >60 distinct lipid species. We show that Piezo2 alters its local membrane composition such that it becomes enriched with specific lipids, such as phosphoinositides, and forms specific, long-term interactions with a variety of lipids at functionally relevant sites.**

## Introduction

Piezo1 and Piezo2 are membrane-embedded mechanosensitive ion channels that play diverse and critical roles in mammalian physiology and pathology (Lai et al., 2022; Coste et al., 2010). Widely expressed across tissue and cell types, Piezo1 is required for blood pressure regulation and vascular development (Li et al., 2014; Ranade et al., 2014a; Zeng et al., 2018) and a common polymorphism of the channel is known to confer protection against severe malaria (Ma et al., 2018; Nguetse et al., 2020). Piezo2 is responsible for conveying tactile pain (Murthy et al., 2018; Szczot et al., 2018), gentle touch sensations (Zhang et al., 2019), and proprioception (Woo et al., 2015). These membrane-embedded force sensors are essential in mammals, as knockout studies show that the absence of Piezo1 or Piezo2 is lethal in mice (Dubin et al., 2012; Li et al., 2014; Ranade et al., 2014a). Malfunction of Piezo channels resulting from gain-of-function (GOF) and loss-of-function (LOF) mutations have been shown to lead to various types of disorders. These include hereditary xerocytosis (Piezo1, GOF; Glogowska et al., 2017), generalized lymphatic dysplasia (Piezo1, LOF; Fotiou et al., 2015), distal arthrogryposis 5 (Piezo2, GOF; Coste et al., 2013; McMillin et al., 2014), Gordon syndrome (Piezo2, GOF; McMillin et al., 2014; Alisch et al., 2017), and Marden-Walker Syndrome (Piezo2, GOF; McMillin et al., 2014). Additionally, a Piezo2 LOF phenotype in

humans is characterized by loss of discriminative touch and proprioception leading to ataxia and dysmetria (Chesler et al., 2016). Similarly, conditional knockout of Piezo2 in mice neurons abrogates light-touch sensation (Ranade et al., 2014b).

As membrane proteins, Piezo1 and Piezo2 affect and are affected by the behavior of the surrounding lipid environment. In a cryo-EM structure, Piezo1 was shown to induce local curvature within a liposome, and it is thought that this curvature is critical in allowing both Piezo1 and Piezo2 to sense mechanical forces (Lin et al., 2019; Shin et al., 2019). Additionally, Piezo1 can activate when reconstituted into liposomes or isolated in membrane blebs free from cytoskeleton, suggesting that it can be gated via a force-from-lipids mechanism (Cox et al., 2016; Syeda et al., 2016). However, it is possible that Piezo1 gating is modulated by the extracellular matrix or cytoskeletal elements (Gottlieb and Sachs, 2012; Cox et al., 2016; Bavi et al., 2019; Romero et al., 2020). In contrast, there is emerging evidence that Piezo2 requires cytoskeletal elements to activate (Eijkelkamp et al., 2013; Romero et al., 2020), suggesting different modes of activation for Piezo2 (Moroni et al., 2018; Shin et al., 2019).

Individual membrane lipids can regulate the activity and function of membrane proteins, either through direct lipid–protein interactions (Gimpl et al., 1997; Deleu et al., 2014;

<sup>1</sup>Research School of Biology, Canberra, Australia.

Correspondence to Ben Corry: [ben.corry@anu.edu.au](mailto:ben.corry@anu.edu.au).

This work is part of a special issue on mechanotransduction by membrane proteins.

© 2022 Lin et al. This article is distributed under the terms of an Attribution–Noncommercial–Share Alike–No Mirror Sites license for the first six months after the publication date (see <http://www.rupress.org/terms/>). After six months it is available under a Creative Commons License (Attribution–Noncommercial–Share Alike 4.0 International license, as described at <https://creativecommons.org/licenses/by-nc-sa/4.0/>).

Montenegro et al., 2017) or indirectly by altering bulk membrane properties (Mitchell et al., 1990; Gimpl et al., 1997; Ridone et al., 2020). Experimental studies of Piezo channels have highlighted the important interplay between membrane lipids and the protein in modulating its function (Cox and Gottlieb, 2019). Depletion of phosphoinositides via TRPV1 is known to inhibit both Piezo1 and Piezo2 activity (Borbiro et al., 2015). There is also specific evidence for a role of phosphatidylinositol biphosphate (PIP2) in activating Piezo2 (Narayanan et al., 2018). Additionally, dietary fatty acids have been shown to play roles in modulating Piezo channel function, with margaric acid inhibiting both Piezo1 and Piezo2 function (albeit at higher concentration for Piezo2) and polyunsaturated (PUS) fatty acids modulating Piezo1 inactivation (Romero et al., 2019; Zheng et al., 2019; Romero et al., 2020). Piezo channels are also regulated by cholesterol (CHOL). Depletion and disruption of membrane CHOL affects the organization of Piezo1 clusters, leading to slowing of activation and disruption of inactivation (Ridone et al., 2020). Additionally, the CHOL binding STOML3 has been shown to modulate Piezo1 and Piezo2 sensitivity by modulating membrane stiffness (Qi et al., 2015a).

Structurally, Piezo1 and Piezo2 are formed from three subunits that arrange as three long propellers extending in a domed structure from a central pore (Fig. 1; Zhao et al., 2018; Wang et al., 2019). Each propeller contains nine transmembrane helical units (THUs), each formed by a bundle of four transmembrane (TM) helices. The innermost helices, TM 37 (outer helix [OH]) and TM 38 (inner helix [IH]), from each monomer trimerize to form the pore together with the anchor, large extracellular cap, and C-terminal domain. A long helical beam 9 nm long supports each propeller on the intracellular side, bridging them to the central pore module.

Using computational techniques, several recent studies have characterized the lipid fingerprint of Piezo1 (the way in which the protein modulates its lipid environment), revealing several functionally important PIP and CHOL binding sites (Buyan et al., 2020; Chong et al., 2021; Jiang et al., 2021). For example, the deletion of four lysine residues in a prominent PIP binding site (4K site) near TM 37 was seen to abolish inactivation in electrophysiological experiments (Buyan et al., 2020). Simulations were also able to reproduce a CHOL binding site in the anchor region of Piezo1, first identified by crosslinking data (Hulce et al., 2013; Buyan et al., 2020). Both sites are conserved in Piezo2 and may serve as important lipid binding sites.

Given the structural similarities and 42% sequence homology between Piezo1 and Piezo2, it is hypothesized that Piezo2 would similarly induce doming of the membrane. Additionally, it would be interesting to see how the lipid fingerprint of Piezo2 differs from Piezo1, and whether key PIP and CHOL binding sites on Piezo1 are conserved in Piezo2. Computational inquiries into the lipid-protein interactions of Piezo2 have been hampered by the absence of structural data until recently, when the structure of Piezo2 was solved by Wang et al. (2019) to a resolution of 3.8 Å. Consisting of ~2,800 residues, Piezo2 is slightly larger than Piezo1, but most of these additions occur in extracellular membrane loops. Here, we use coarse-grained (CG) MD simulations to characterize the lipid fingerprint of the Piezo2 protein in

a complex mammalian membrane, highlighting its notable similarities to the published Piezo1 lipid fingerprint. We note the presence of conserved, high-occupancy binding sites for PIPs and CHOL on the protein, as well as several other lipid binding sites of interest.

## Materials and methods

### System setup

Simulations were set up and run using GROMACS 2019.3 (Van Der Spoel et al., 2005) and the Martini 2.2 forcefield (Marrink et al., 2007; de Jong et al., 2013). The cryo-EM structure of mPiezo2 (mouse Piezo2, PDB accession no. 6KG7) solved by Wang et al. (2019) was obtained from the PDB, and glycans were removed. The CHARMM-GUI Martini Maker was used to build in the five short unresolved loops per monomer (<20 residues) and coarse grain the structure with an elastic network cutoff of 0.9 nm (Periole et al., 2009; Qi et al., 2015b). Long unresolved loop regions were omitted from the model (details of the final model used are in Table S1). Using the INSANE python script (Wassenaar et al., 2015), Piezo2 was embedded in a 50 × 50-nm average mammalian membrane model containing 63 different lipid species (exact lipid composition detailed in Table S2; Ingólfsson et al., 2014), solvated, and ionized with 0.15 M NaCl. The final system has dimensions 50 × 50 × 20 nm and contains ~400,000 particles, with ~290,000 of these being solvent beads and ~7,500 ion beads.

All simulations were carried out at 310°K (maintained using a velocity-rescale thermostat; Bussi et al., 2007) with a van der Waals radius of 1.1 nm. The system was energy minimized using the steepest descent method for 1,000 steps. The system was simulated in the constant pressure, constant volume (NVT) ensemble at 1 atm for 10 ps with backbone position restraints (1,000 kJ mol<sup>-1</sup> nm<sup>-2</sup>) using a 2-fs timestep. Following this, three position-restrained (1,000 kJ mol<sup>-1</sup> nm<sup>-2</sup>) constant number of particles, pressure, and temperature (NPT) equilibration simulations with 5-, 10-, and 20-fs timesteps were run for 5,000 steps each, with a pressure of 1 atm maintained using a Berendsen barostat with semi-isotropic conditions (Berendsen et al., 1984). Production simulations were carried out for 21 μs in triplicate using a 20-fs timestep, with the backbone beads weakly restrained to their starting conformations using a force constant of 50 kJ mol<sup>-1</sup> nm<sup>-2</sup> to prevent unrealistic protein deformation.

### Simulation analysis

Unless otherwise specified, all analysis was carried out using the last 7 μs of the trajectory, with one frame representing 1 ns of simulation time. Lipid depletion/enrichment (D/E) analysis was performed using the formula and script detailed in Buyan et al. (2020), which is a modified version of the original script from Corradi et al. (2018). This script can be downloaded from <http://cgmartini.nl/index.php/tools2/proteins-and-bilayers> under “Analyse Lipid Fingerprints.” The cutoff used for D/E was 20 Å. Lipid contact analysis was carried out using the Visual Molecular Dynamics contactFreq tcl script, with lipid occupancies calculated individually for each monomer in each replicate to provide a total of nine occupancy values from which the average is reported. Graphs were generated using Matplotlib. Representative

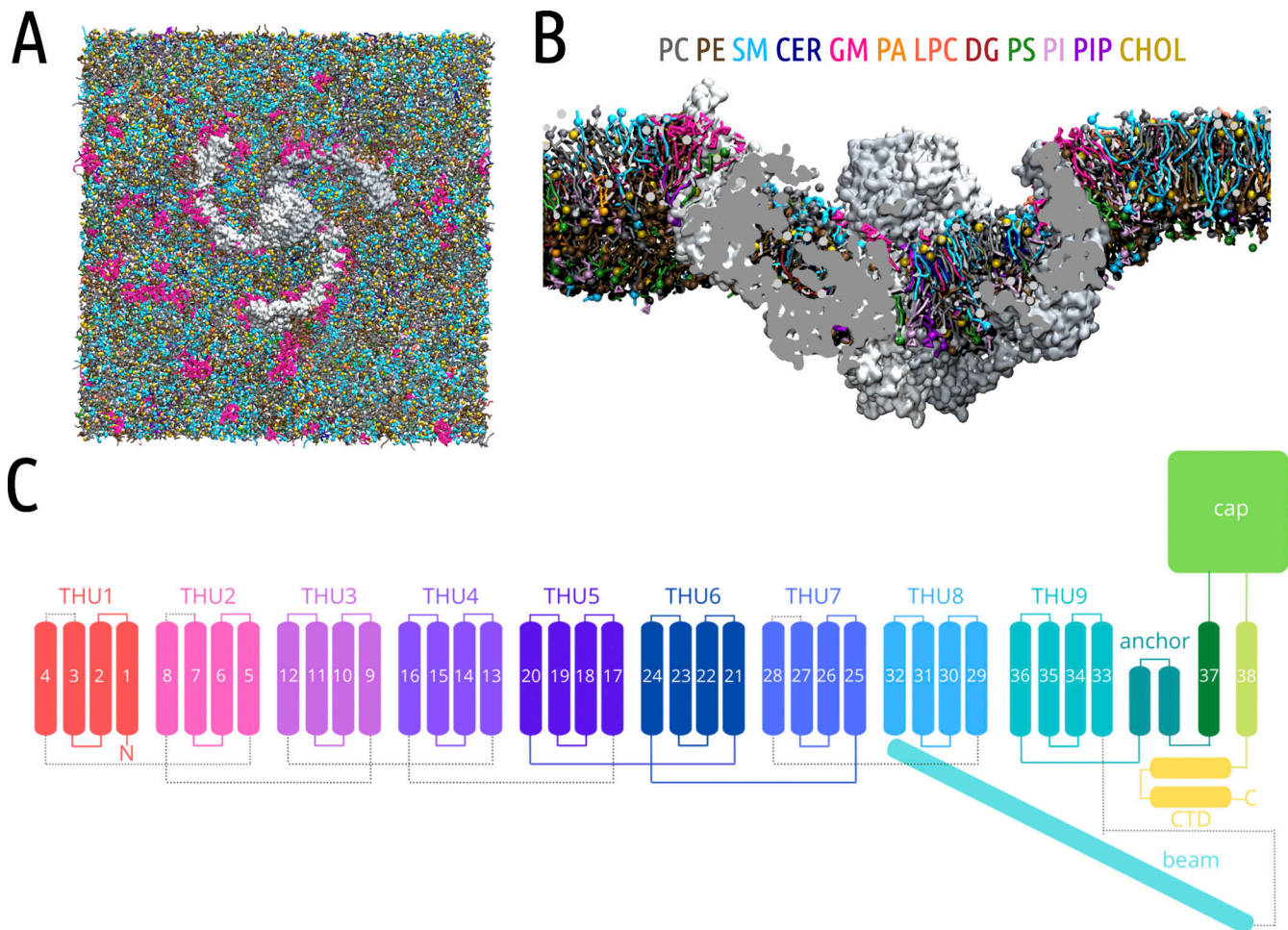


Figure 1. **Piezo2 in a complex mammalian membrane after equilibration.** (A) Top-down view of Piezo2 embedded in a 63-component realistic mammalian membrane. The protein is shown in white, and lipids are colored according to headgroup type as shown in B. (B) Side-on view of Piezo2, with water, ions, lipid, and protein in front of the clipped plain omitted from the visualization for clarity. (C) Topology of the 38 helices in the Piezo2 structure, including the anchor, cap, and C-terminal domain (CTD); dotted lines indicate unresolved regions not modeled in our simulations.

snapshots of the simulation system and key binding sites were generated using Visual Molecular Dynamics (Humphrey et al., 1996). Lipid density maps were produced using gmx densmap, with densities averaged across all z values (both leaflets) and plotted using an in-house Python script. Statistical differences between lipid D/E were calculated using Student's *t* tests; paired, two-tailed *t* tests were used when comparing lipids in the same simulation system, and unpaired, two-tailed *t* tests were used to compare lipids between replicate systems. Differences in occupancy between negative lipids on positively charged residues of Piezo2 were calculated and evaluated using a one-way ANOVA with Tukey's post hoc test.

#### Online supplemental material

Fig. S1 shows changes in lipid D/E index over time. Fig. S2 gives details on PUS D/E behavior around Piezo2. Fig. S3 shows time series data tracking PIP binding across the individual monomers. Figs. S4 and S5 show density maps and lipid contacts on the Piezo2 structure for lipid types not discussed in the main article. Fig. S6 shows the locations of disease-causing mutations along with the lipids that interact at these residues on Piezo2.

Table S1 contains information on the Piezo2 model used in our simulations. Table S2 details the membrane lipid composition. Table S3 contains information regarding lipid interactions at disease-causing mutations.

## Results

### PIPs, glycolipids (GM), DGs, and PUS lipids are enriched around Piezo2

A CG model of Piezo2 was embedded in a complex, asymmetric mammalian membrane containing 63 distinct lipid species (composition detailed in Table S2) and simulated for 21  $\mu$ s in triplicate (Fig. 1 A) to facilitate characterization of its lipid fingerprint. An average mammalian membrane was used to reflect the physiological lipid environment of Piezo2 and facilitate comparisons to the published Piezo1 lipid fingerprint (Buyan et al., 2020). Its composition is described in Ingólfsson et al. (2014), and was based on mass spectrometry data from Madin-Darby canine kidney cells (a model mammalian cell line) and human erythrocyte plasma membranes (Han and Gross, 1994; Virtanen et al., 1998; Sampaio et al., 2011). The bilayer used

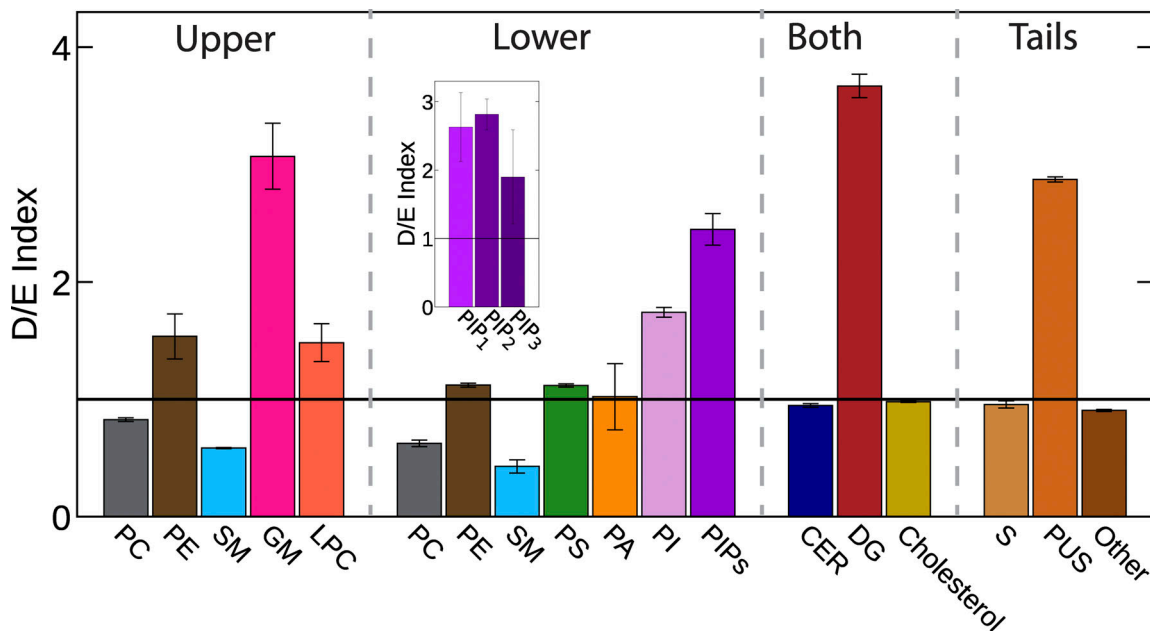


Figure 2. Lipid D/E index by headgroup, calculated across the final 7  $\mu$ s (14–21  $\mu$ s) and averaged between the three replicates. SEMs are indicated using error bars. The D/E index for each PIP species is included as an inset.

contains phosphatidylcholine (PC), phosphatidylethanolamine (PE), sphingomyelin (SM), ceramides (CER), diacylglycerol (DG), and CHOL in both leaflets, with GM and lysophosphatidylcholines (LPC) present in the upper leaflet only, and phosphatidylserine (PS), phosphatidic acid (PA), phosphatidylinositol (PI), and PIP in the lower leaflet only. Multiple lipid species are included in each headgroup category, with lipid tails that differ in length and number of unsaturations. Lipids with no C=C double bonds in their tails were classified as saturated, while lipids with more than one unsaturation on each tail were classified as PUS. Finally, lipids that contain only one saturation on either tail were grouped into the “other” category.

Piezo2 is initially embedded in a flat bilayer; however, within the first 200 ns of each replicate simulation, a lipid dome forms around Piezo2 (Fig. 1 B) and remains for the duration of the simulation. To characterize the lipid annulus around Piezo2, we calculated the D/E index of each lipid type, categorized by either headgroup or lipid tail type, around the protein (Fig. 2). D/E index values >1 indicate enrichment of the lipid type around the protein compared with its concentration in the bulk membrane, whereas values <1 suggest depletion of the lipid. We tracked the D/E index of each lipid type over the 21  $\mu$ s of simulation time (Fig. S1) to assess whether sufficient time for equilibration occurred, since lateral lipid diffusion takes place on the order of microseconds, and other key events such as dome formation occur more rapidly. We observed that high-concentration lipid species that are present in both leaflets (CHOL, SM, PC, and PE) had D/E indices that stabilized rapidly, in <4  $\mu$ s. In contrast, lower-concentration lipid species (DG, LPC, GM, CER, PI, PA, PIPs, and PS) required  $\leq$ 14  $\mu$ s for the lipid D/E index to stabilize.

When the D/E index was calculated across the final 7  $\mu$ s of each replicate and aggregated, we noted the relative enrichment of DG, GM, PIPs, PI, LPC, and PE (descending order) around

Piezo2. Given the functional roles played by PIPs in modulating Piezo channel function, we further examined the D/E indices of phosphatidylinositol phosphate (PIP1), PIP2, and phosphatidylinositol trisphosphate (PIP3) individually (Fig. 2, inset). This showed that Piezo2’s lipid annulus was enriched in all PIPs, with no statistical difference between D/E indices of individual PIP species. PC and SM lipids were observed to be depleted around Piezo2. CHOL, PS, and CER had D/E indices close to 1, indicating similar lipid concentrations in the bulk membrane and around the protein. When lipid species were categorized according to tail saturation rather than headgroup, we observed significant enrichment of PUS lipids around Piezo2. When the D/E index of individual PUS species was quantified (Fig. S2), we noted that all lipids containing PUS tails were enriched around the protein, with DAPE (PE headgroup, C20:4/C22:5 tails) having the highest enrichment around the protein in the upper leaflet and DUPs (PS headgroup, C20:5/C22:6 tails) being most enriched in the lower leaflet.

### PIPs form specific and long-lasting interactions with the lower region of Piezo2

Given their relative enrichment around Piezo2 and evident modulatory action on Piezo channels (Borbiro et al., 2015; Narayanan et al., 2018), we sought to better understand the nature of the PIP–Piezo2 interactions formed in our simulations. A 2-D density map (Fig. 3 A) shows that PIPs are generally homogeneously distributed in the bulk membrane, with evidence of hotspots around the protein suggesting the presence of specific PIP binding sites on Piezo2. These sites are mapped onto the structure in Fig. 3 B, in which the backbone of Piezo2 is shown and each residue colored according to occupancy of PIP lipids around it. Dark purple regions, indicating areas of high PIP occupancy, are visible along the cytosolic side of the protein,

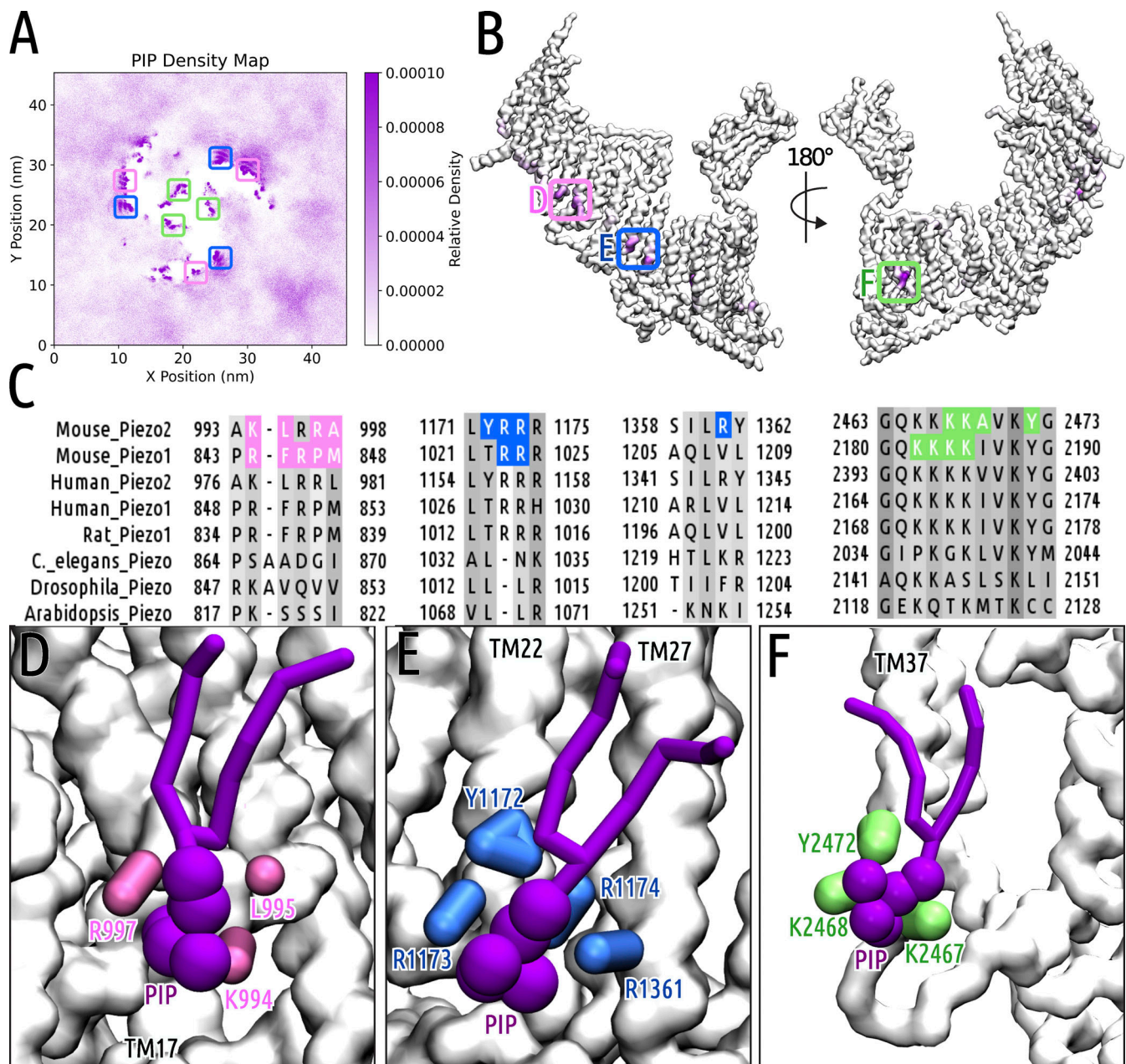


**Figure 3. Protein–lipid interactions between PIPs and Piezo2.** (A) Density map of PIP species around Piezo2. (B) PIP binding sites mapped onto the Piezo2 structure, with darker coloration indicating higher occupancy of PIPs around the given residue. (C) Top three PIP binding sites mapped onto Piezo multiple sequence alignment. (D) First PIP binding site. (E) Second PIP binding site. (F) Third PIP binding site. The residues on Piezo2 coordinating PIP binding are shown in pink, blue, or green surface, respectively. PIP species are represented by purple licorice and spheres. The protein backbone is represented by a white surface.

consistent with the presence of PIPs in the intracellular leaflet only. From this, three high (>40%) PIP occupancy sites were identified (Fig. 3, D–F) and shown to be conserved in Piezo1 (Fig. 3 C). Time series plots (Fig S3) show the rate of binding and unbinding as well as the competition of lipids for these sites (discussed in more detail below).

PIP binding site D is located on TM17 of THU5 on Piezo2, toward the middle of each propeller (Fig. 3, A and B, pink). In the snapshot (Fig. 3 D), the PIP lipid headgroup can be seen interacting with two positively charged residues (K994 and R997) on the protein, as well as a nonpolar (L995) amino acid. This binding

site is strongly conserved between Piezo2 and Piezo1, with all four homologous residues on Piezo1 also known to bind PIP.

PIP binding site E is located on TM22 (THU6) and TM27 (THU7) of Piezo2 and consists of three positively charged residues (R1173, R1174, and R1361) that coordinate the binding of the PIP headgroup as well as Y1172, which interacts with PIP at the lipid tail moiety close to the headgroup.

Finally, PIP binding site F is in the linker region of Piezo2, between the anchor domain and the OH of the pore. This site is homologous to the 4K PIP binding site identified on Piezo1 (Buyan et al., 2020). It consists of two adjacent, positively

charged residues (K2467 and K2468) that coordinate the headgroup of bound PIP lipids and two nonpolar residues (A2669 and Y2472).

### Key CHOL binding sites on Piezo2

CHOL is an important component of the lipid membrane, not only in modulating membrane properties (Mitchell et al., 1990; Gimpl et al., 1997; Ridone et al., 2020) but also in regulating behavior of membrane proteins (Gimpl et al., 1997; Deleu et al., 2014; Montenegro et al., 2017). As CHOL has been shown to have an intimate yet complicated relationship with Piezo1's function (Ridone et al., 2020; Chong et al., 2021), it follows that CHOL likely has a similar relationship with Piezo2. There is no enrichment of CHOL around Piezo2, as its D/E index is  $\sim 1$ . However, there are several interaction sites around Piezo1, as shown by the density map in Fig. 4 A. Looking at these sites on the structure of Piezo2 (Fig. 4 B), there are several CHOL binding sites with high occupancy (Fig. 4 B), and the three highest occupancy sites are discussed in detail here.

CHOL binding site D is located at the N terminus of the protein and comprises M1, A2, and V5, while binding site E can be found on TM5 and TM8 (THU 2), containing residues K212, Y346, and T350. We note that both sites are in the first three THUs of Piezo2, which is not resolved in the Piezo1 structure (indicated by pale pink coloring on sequence alignment). Therefore, we cannot comment on whether these CHOL binding sites are conserved on Piezo1. Binding site F is located on TM33 and TM36 of the protein in THU9 of the protein, close to the pore. At this site, we observe four amino acids (V2269, I2273, L2364, and V2368) that coordinate the binding of a CHOL molecule. This site is conserved in Piezo1, with I1989 known to also bind CHOL. Additionally, we note that residues within the LVPF motif in the anchor domain of both Piezo1 and Piezo2, identified to interact with CHOL by previous crosslinking studies (Hulce et al., 2013), also have high CHOL occupancy (>50%) in our simulations; however, this was not among the top three ranked CHOL binding sites.

### Other lipids also form long-lasting interactions with Piezo2

In addition to CHOL and PIPs, which have been experimentally shown to modulate the function of Piezo channels, we analyzed the distribution of other lipids present in the mammalian membrane around Piezo2 (Figs. S4 and S5) to identify key lipid protein interactions that may be functionally relevant.

Density maps of each lipid headgroup (Figs. S4 and S5, left) show that most lipids are generally homogeneously distributed in the membrane, with some lipid aggregation around Piezo2 noted for all lipid types (PE, GS, LPC, PA, PS, PI, DG, and CER) except PC and SM. Generally, we observe symmetric distribution of lipids around each monomer of the trimeric protein, with many lipid density hotspots seen across all three arms in similar locations. This indicates relatively good convergence of lateral lipid diffusion in our simulations. Depletion of SM lipids (noted previously) around Piezo2 results in a wider region of white around the protein, indicating low density throughout the simulation (Fig. S4 E). In contrast, the density map for GM lipids (Fig. S4 G) indicates that they self-cluster in the bulk membrane

and form patches of high density around the protein. We then calculated the percentage of simulation time that a specific lipid type was near Piezo2 on a per-residue basis and mapped these occupancy values onto the protein structure (Figs. S4 and S5, right). Unsurprisingly, lipids that are confined to the lower leaflet (PA, PS, and PI) form contacts with residues on the cytosolic side of the protein, whereas lipids present only in the upper leaflet (GM and LPC) have areas of high occupancy toward the top of Piezo2. Despite being present in both leaflets, PC lipids mostly form contacts with the upper portion of Piezo2, whereas PE lipids primarily interact with the lower portion of the protein. This result is consistent with the asymmetric concentrations of PC (higher in the upper leaflet) and PE (higher in the lower leaflet) lipids between leaflets. CER and DG lipids, which are present in both leaflets, interact with Piezo2 across several sites scattered across the protein.

By visualizing the residues with the highest occupancy of each lipid type on the protein, we identified some intriguing high-occupancy binding sites for SM, PI, and DG on Piezo2. Despite overall depletion of SM around Piezo2, we note the presence of a high-occupancy hotspot in the IH of the pore (Fig. 5, B and D), which results from the binding of SM lipids on the interface between two monomers to residue F2758 (on one arm) and S2760 (on the adjacent arm). While PI lipids bind to multiple locations on the protein, the site with the highest occupancy shows PI stabilized by two lysine residues (K735 and K738) and one tyrosine residue (Y739) in TM14. Finally, we note a high-occupancy site for DG observed in the middle of the propeller (Fig. 5, B and E). This site contains predominantly aromatic residues from TM25, TM29, and TM32 of the protein, which form stabilizing interactions with the headgroup of DG.

### Selective binding of negative lipids to Piezo2

All negative lipids display localized binding sites on the protein, which represent competition for basic residues on the protein. As shown in Fig. 6, different negative lipids are seen to bind to arginine and lysine residues on the protein. Many of these sites display a preference for some lipid types over others, with several showing statistically significant differences in occupancy compared with all other negative lipids. In particular, we note the presence of four PI selective residues (R536, K735, K738, and K1129) of which two (K735 and K738) comprise part of the PI binding site (Fig. 5 D) discussed in the previous section. Additionally, all PIP binding sites identified (Fig. 3, D–F) contain positively charged residues that are selective for PIP over all other lipids (R997, R1173, R1174, R1361, and K2468). These represent the sites with the greatest net charge (three or four basic residues) that likely select for PIPs as the most highly charged negative lipid. The preference of PI or PIPs for these sites is notable given the much larger number of PS lipids present in the simulation system (Table S2). Finally, we note the presence of a single PS selective residue (K1185) located on TM23 of the protein.

## Discussion

Mechanosensitive Piezo channels perform diverse, important roles in humans, and their dysfunction has been implicated in a

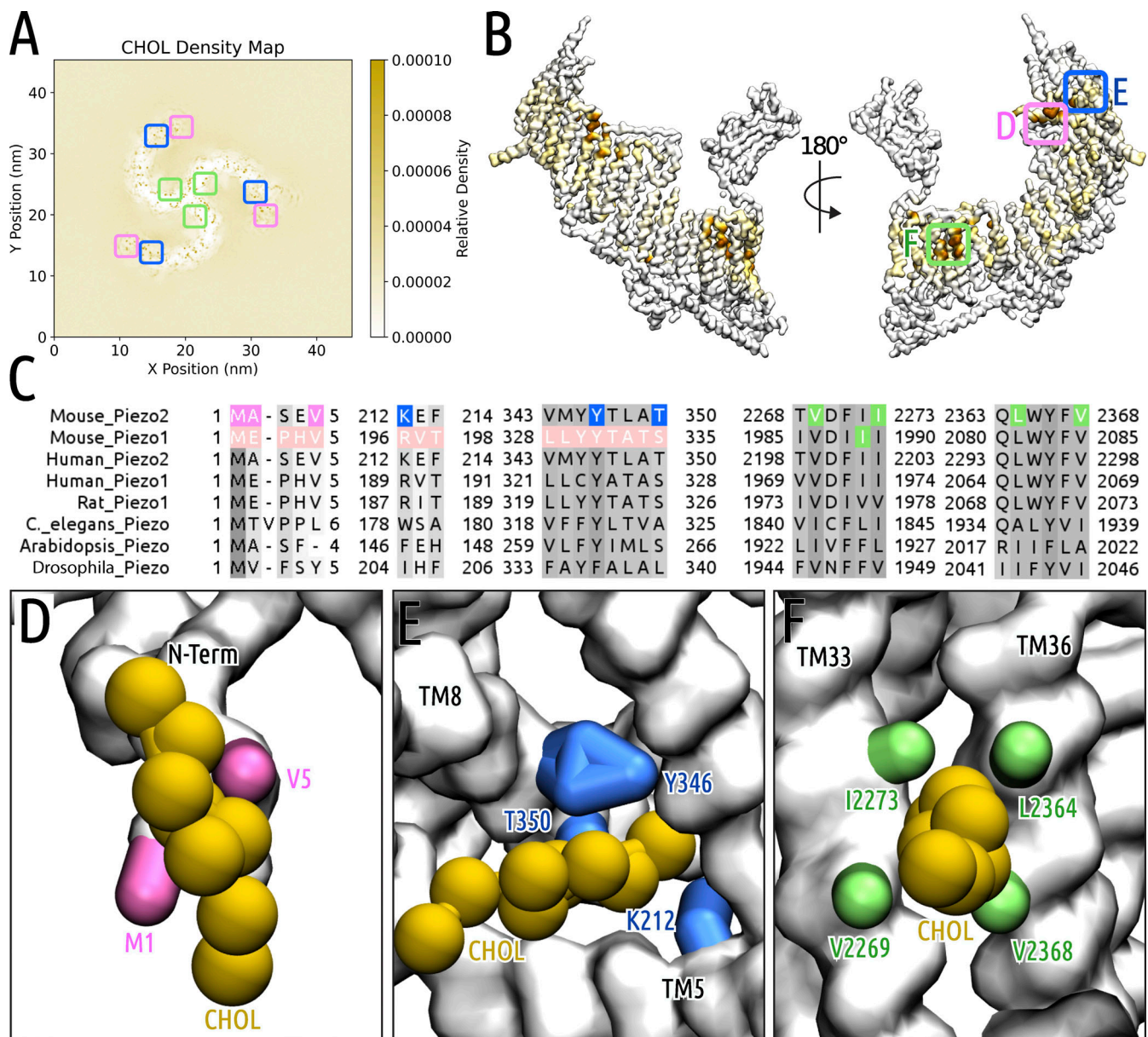


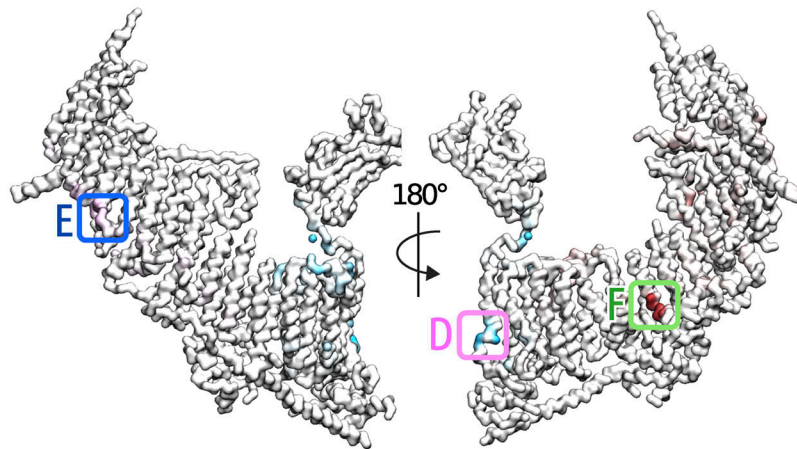
Figure 4. **Protein-lipid interactions between CHOL and Piezo2.** (A) Density map of CHOL species around Piezo2. (B) CHOL binding sites mapped onto the Piezo2 structure, with darker coloration indicating higher occupancy of CHOL around the given residue. (C) Top three CHOL binding sites mapped onto Piezo2 multiple sequence alignment. (D) First CHOL binding site. (E) Second CHOL binding site. (F) Third CHOL binding site. The residues on Piezo2 coordinating CHOL binding are shown in pink, blue, or green surface, respectively. CHOL species are represented by yellow spheres. The protein backbone is represented by a white surface.

range of genetic disorders. As Piezo1 and Piezo2 are membrane-embedded channels, it is unsurprising that their function is regulated by the local lipid environment. Several recent computational studies have characterized the lipid fingerprint of Piezo1 and highlighted the critical roles which lipids such as CHOL and PIP2 play in modulating its behavior (Buyan et al., 2020; Chong et al., 2021; Jiang et al., 2021). Here, we carried out CG MD simulations of Piezo2 embedded in a complex mammalian membrane to examine its local lipid environment and identify key lipid binding sites to compare its lipid fingerprint directly with Piezo1. In our simulations, GM, PIP, DG, and PUS lipids are enriched around Piezo2, while PC and SM lipids are depleted around

the protein. Additionally, we note several key PIP and CHOL interactions with Piezo2 that independently arise in multiple replicates and persist for much of the simulation time.

Compared to Piezo1 (Buyan et al., 2020), the lipid fingerprint of Piezo2 is similar. Both proteins show enrichment of PUS lipids, DG, PIPs, PI, GMs, LPC, and PEs and depletion of PC and SM. However, there are some notable differences in the lipid enrichment between Piezo1 and Piezo2. One of the most striking is that PIPs are significantly more enriched in Piezo1 than Piezo2 ( $P < 0.0001$ ; Fig. 2). There is no statistically significant difference in the D/E index of PIP species for either Piezo1 or Piezo2 (Fig. 2, inset). For both Piezo1 and Piezo2, the differences

A



B

Mouse_Piezo2	2758	F F S G	2761	735	K I L K Y F	740	1308	V I I F S Y L F W F V	1318	1984	M Y N	1986	1984	M Y N	1986
Mouse_Piezo1	2484	F F S E	2487	630	K L L R V F	635	1155	V A V F R Y L F W L V	1165	1679	G Y Q	1681	1679	G Y Q	1681
Human_Piezo2	2688	F F S G	2691	731	K I L K Y F	736	1291	V I I F S Y L F W F V	1301	1914	M Y N	1916	1914	M Y N	1916
Human_Piezo1	2458	F F S E	2461	624	K L L K A F	629	1160	V A V F R Y L F W L V	1170	1679	V Y Q	1681	1679	V Y Q	1681
Rat_Piezo1	2472	F F S D	2475	621	K L L R V F	626	1146	V A V F R Y L F W L V	1156	1666	M Y Q	1668	1666	M Y Q	1668
C_elegans_Piezo	2375	I F T T	2378	682	G L A Y A F	687	1164	S F V F H Y G H W I T	1174	1606	V V N	1608	1606	V V N	1608
Arabidopsis_Piezo	2397	Q C S D	2400	681	E T K R R L	686	1204	L Y C Y V H L L D V V	1214	1595	I W S	1597	1595	I W S	1597
Drosophila_Piezo	2458	F I G G	2461	638	K I M Y G F	643	1150	N G V L C G F Y W F T	1160	1720	S W Y	1722	1720	S W Y	1722

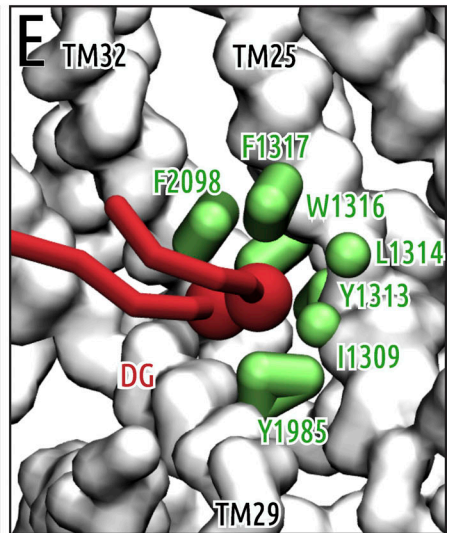
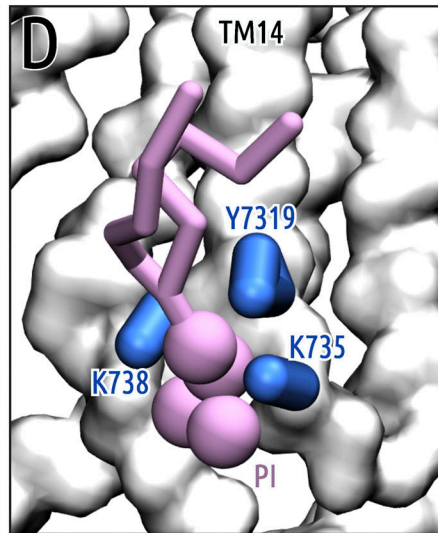
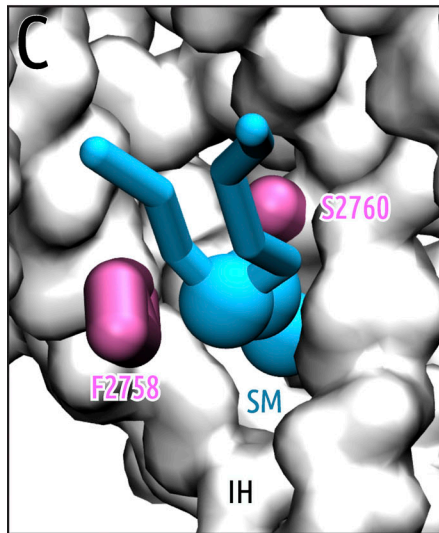


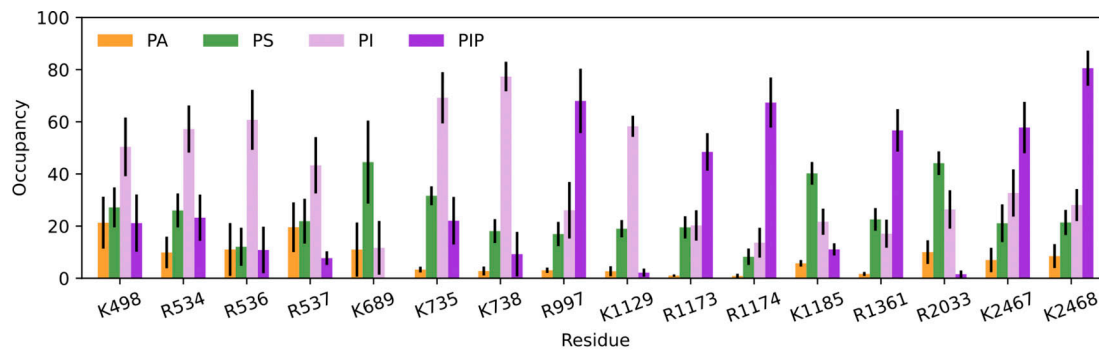
Figure 5. **Selected binding sites of other lipids to Piezo2.** (A) Structure of Piezo2 with lipid binding sites highlighted on the structure as pink, blue, or green boxes. This figure is an amalgamation of images in Figs. S4 and S5 to show the relation of these different binding sites to each other. (B) Sequence of Piezo2 with key lipid interactions highlighted on it. (C–E) The binding sites visualized in C–E are highlighted in a pink (SM binding site), blue (PI binding site), or green (DG binding site) box on the sequence.

between PI and PIP D/E are statistically significant (Piezo1,  $P = 0.0002$ ; Piezo2,  $P = 0.0247$ ). Another notable difference is that for Piezo2, PA lipids are preferred over PS lipids ( $P = 0.0039$ ), whereas in Piezo1, there is no such preference. We also examined the pattern of PUS lipids around Piezo2, as they have been shown to be influential for Piezo channel activity (Romero et al., 2019; Romero et al., 2020). The pattern of PUS lipids around Piezo2 is similar to that of Piezo1 (Fig. S2); however, Piezo2 prefers PE C20:5/C22:6 over PS C20:4/C22:5 ( $P = 0.0171$ ), whereas in Piezo1's fingerprint, the D/E indices are not significantly different ( $P = 0.6170$ ).

PIPs have been shown to play key regulatory roles for a range of membrane proteins (Dickson and Hille, 2019), including for

Piezo channels, where the presence of PIP<sub>2</sub> in the inner leaflet of the membrane is known to promote channel activation (Borbiro et al., 2015; Narayanan et al., 2018). Our simulations reveal PIP binding hotspots scattered across the lower half of Piezo2, consistent with prior studies of Piezo1 showing that PIP binds at the numerous positively charged residues on the intracellular side of the protein. This result is unsurprising, given the conservation of many positively charged lysine and arginine residues between Piezo1 and Piezo2. Previous simulation studies have indicated that PIPs form several functionally important interactions with Piezo1, including at a patch of four lysine residues (K2166–K2169, human sequence numbering) located in





Residue	Significant Differences in Binding	Highest Occupancy Negative Lipid
R534	PA-PI,PI-PIP	PI
R536	PA-PI,PI-PIP,PI-PS	PI*
K735	PA-PI,PI-PIP,PI-PS	PI*
K738	PA-PI,PI-PIP,PI-PS	PI*
R997	PA-PIP,PI-PIP,PIP-PS	PIP*
K1129	PA-PI,PA-PS,PI-PIP,PI-PS,PIP-PS	PI*
R1173	PA-PIP,PI-PIP,PIP-PS	PIP*
R1174	PA-PIP,PI-PIP,PIP-PS	PIP*
K1185	PA-PI,PA-PS,PI-PS,PIP-PS	PS*
R1361	PA-PIP,PI-PIP,PIP-PS	PIP*
R2033	PA-PS,PI-PIP,PIP-PS	PS
K2467	PA-PIP,PIP-PS	PIP
K2468	PA-PIP,PI-PIP,PIP-PS	PIP*

Figure 6. **Occupancies of negative lipids between arginines and lysines that have displayed >50% occupancy in PA, PS, PI, or PIPs; differences in lipid occupancies.** Bar graphs are averages between three replicates, and the error bars are SEM. Table shows statistically significant differences in lipid occupancies as determined by a one-way ANOVA with Tukey's post hoc test. Residues that selectively bind a specific negatively charged lipid are indicated with an asterisk.

the intracellular linker between the pore and propeller domains. A variant of Piezo1 without these four residues abolishes inactivation and leads to xerocytosis (Albuisson et al., 2013), while mutation to asparagine or aspartic acid reduces sensitivity to force in addition to delaying inactivation. Buyan et al. (2020) hypothesized that these changes in Piezo1 kinetics can be explained by a combination of structural changes and changes to PIP binding behavior at this 4K site. In our simulations, this PIP binding site is conserved in Piezo2, suggesting that Piezo2 inactivation and pressure sensitivity may be similarly regulated by PIP binding at this site. It has previously been shown experimentally that PIP<sub>2</sub> binds to a Piezo2 peptide sequence containing K735 and K738 (Narayanan et al., 2018). While PIP binding is seen in this position, this is the site that we have shown prefers binding of PI (Fig. 5 E). Additionally, it has previously been suggested that the homologous Piezo1 sequence RKLLRVFWWL does not bind PIP<sub>2</sub>. However, in our simulations, we note that the three residues just to the left of this sequence (TLW) are important for PIP binding at this position, and the lack of binding in the peptide may have been due to their absence. Notably, we see selectivity for different negatively charged lipids at some sites that appears to be controlled by the overall charge of the site. We note that while our CG simulations explicitly represent the three different PIP species (PIP<sub>1</sub>, PIP<sub>2</sub>, and PIP<sub>3</sub>) present in the mammalian membrane, they do not distinguish between phosphate positions within each charge state (e.g., PI(3,5)P<sub>2</sub> versus PI(3,4)P<sub>2</sub>).

CHOL has also been shown to be a key player in Piezo proteins' function (Ridone et al., 2020; Chong et al., 2021). Despite no general enrichment of CHOL around Piezo2 being observed, we noted the presence of several CHOL binding sites on Piezo2. We have identified three sites with high CHOL occupancy. In addition to these, a CHOL binding site previously identified via cross-linking studies containing the RVLV motif on Piezo1 is also highly occupied in our simulations, but was not among the top three. Despite CHOL being shown to regulate Piezo proteins, it is still unclear whether it does so by modulating the membrane properties, through direct protein-lipid interactions, or a mixture of both. A few disease-causing mutations in Piezo2 occur at locations with consistent lipid binding (Fig. S6 and Table S3). While changes in lipid binding may contribute to altered function, it is difficult to discern this from alternative explanations such as alterations in Piezo2 structure.

Some lipids besides CHOL and PIPs also formed notable interactions with Piezo2. SM has a key binding site on the inner pore helix. This is of note, as a recent paper found that SM alters the pressure sensitivity of Piezo1 (Shi et al., 2020). There are no suggestions in the study for how this would occur; however, the binding site for SM found on the IH is conserved and would suggest a plausible explanation. Experimental mutagenesis of residues in this site for both Piezo1 and Piezo2 would confirm this speculation. The other two sites of note were for DGs and PIs. The DG site contained residues from three different helices

and involved two helical repeats. DG could be aiding Piezo2 in signaling in this site; however, without experimental evidence, this remains speculative at best. For the PI site, this is out on the fourth helical repeat of Piezo2. While this could be a case of lysines attracting PIs, it could also be of functional relevance, as mutations outside of the pore region have been shown to contribute to disease (Coste et al., 2013; McMillin et al., 2014; Okubo et al., 2015). Overall, while these lipid sites are of note, only the SM has the clearest possible link to affecting the function of Piezo1, and by proxy that of Piezo2.

Protein–lipid interactions are key for regulating membrane proteins, and the overall membrane environment also influences membrane proteins' behavior. We have found several likely binding sites of CHOL and PIP2, with a smattering of other protein–lipid interactions. A good deal of the lipid binding sites between Piezo1 and Piezo2 are conserved, which suggests there are likely similarities in how they are activated. These lipid binding sites occur around disease-causing mutations (Fig. S6). However, it is difficult to delineate if these mutations are the results of changes in lipid binding, changes in Piezo2's ability to function, or a combination of the two. Further sterol cross-linking experiments on Piezo2 would also aid in showing any relevant CHOL binding sites. Experimental mutagenesis studies could aid in validating the functional relevance of these key lipid binding sites. Electrophysiology, as well as cryo-EM structures of these mutants, may help to shed light on how exactly these mutations are affecting the behavior of Piezo2.

## Acknowledgments

Crina Nimigean served as editor.

We acknowledge funding from the Australian Government through the Australian Research Council (DP200100860). This research was undertaken with the assistance of resources and services from the National Computational Infrastructure (NCI), which is supported by the Australian Government, including support through the Australasian Leadership Computing Grants scheme.

The authors declare no competing financial interests.

Author contributions: Y. Lin, Conceptualization, Investigation, Methodology, Formal Analysis, and Writing - Original Draft; A. Buyan, Conceptualization, Investigation, Methodology, Formal Analysis, and Writing - Original Draft; B. Corry, Conceptualization, Supervision, Writing - Review & Editing, and Funding Acquisition.

Submitted: 23 November 2021

Revised: 22 May 2022

Accepted: 1 July 2022

## References

Albuisson, J., S.E. Murthy, M. Bandell, B. Coste, H. Louis-Dit-Picard, J. Mathur, M. Fénéant-Thibault, G. Tertian, J.-P. de Jaureguiberry, P.-Y. Syfuss, et al. 2013. Dehydrated hereditary stomatocytosis linked to gain-of-function mutations in mechanically activated PIEZO1 ion channels. *Nat. Commun.* 4:1884. <https://doi.org/10.1038/ncomms2899>

Alisch, F., A. Weichert, K. Kalache, V. Paradiso, A.C. Longardt, C. Dame, K. Hoffmann, and D. Horn. 2017. Familial Gordon syndrome associated

with a PIEZO2 mutation. *Am. J. Med. Genet. A.* 173:254–259. <https://doi.org/10.1002/ajmg.a.37997>

Bavi, N., J. Richardson, C. Heu, B. Martinac, and K. Poole. 2019. PIEZO1-mediated currents are modulated by substrate mechanics. *ACS Nano.* 13:13545–13559. <https://doi.org/10.1021/acsnano.9b07499>

Berendsen, H.J.C., J.P.M. Postma, W.F. van Gunsteren, A. DiNola, and J.R. Haak. 1984. Molecular dynamics with coupling to an external bath. *J. Chem. Phys.* 81:3684–3690. <https://doi.org/10.1063/1.448118>

Borbiro, I., D. Badheka, and T. Rohacs. 2015. Activation of TRPV1 channels inhibits mechanosensitive Piezo channel activity by depleting membrane phosphoinositides. *Sci. Signal.* 8:ra15. <https://doi.org/10.1126/scisignal.2005667>

Bussi, G., D. Donadio, and M. Parrinello. 2007. Canonical sampling through velocity-rescaling. *J. Chem. Phys.* 126:014101. <https://doi.org/10.1063/1.2408420>

Buyan, A., C.D. Cox, J. Barnoud, J. Li, H.S.M. Chan, B. Martinac, S.J. Marrink, and B. Corry. 2020. Piezo1 forms specific, functionally important interactions with phosphoinositides and cholesterol. *Biophysical J.* 119:1683–1697. <https://doi.org/10.1016/j.bpj.2020.07.043>

Chesler, A.T., M. Szczot, D. Bharucha-Goebel, M. Čeko, S. Donkervoort, C. Laubacher, L.H. Hayes, K. Alter, C. Zampieri, C. Stanley, et al. 2016. The role of Piezo2 in human mechanosensation. *N. Engl. J. Med.* 375:1355–1364. <https://doi.org/10.1056/NEJMoal602812>

Chong, J., D. De Vecchis, A.J. Hyman, O.V. Povstyan, M.J. Ludlow, J. Shi, D.J. Beech, and A.C. Kalli. 2021. Modelling of full-length Piezo1 suggests importance of the proximal N-terminus for dome structure. *Biophys. J.* 120:1343–1356. <https://doi.org/10.1016/j.bpj.2021.02.003>

Corradi, V., E. Mendez-Villuendas, H.I. Ingólfsson, R.-X. Gu, I. Siuda, M.N. Melo, A. Moussatova, L.J. DeGagné, B.I. Sejdiu, G. Singh, et al. 2018. Lipid-protein interactions are unique fingerprints for membrane proteins. *ACS Cent. Sci.* 4:709–717. <https://doi.org/10.1021/acscentsci.8b00143>

Coste, B., G. Houge, M.F. Murray, N. Stitzziel, M. Bandell, M.A. Giovanni, A. Philippakis, A. Hoischen, G. Riemer, U. Steen, et al. 2013. Gain-of-function mutations in the mechanically activated ion channel Piezo2 cause a subtype of Distal Arthrogyrosis. *Proc. Natl. Acad. Sci. USA.* 110:4667–4672. <https://doi.org/10.1073/pnas.1221400110>

Coste, B., J. Mathur, M. Schmidt, T.J. Earley, S. Ranade, M.J. Petrus, A.E. Dubin, and A. Patapoutian. 2010. Piezo1 and Piezo2 are essential components of distinct mechanically-activated cation channels. *Science.* 330:55–60. <https://doi.org/10.1126/science.1193270>

Cox, C.D., C. Bae, L. Ziegler, S. Hartley, V. Nikolova-Krstevski, P.R. Rohde, C.-A. Ng, F. Sachs, P.A. Gottlieb, and B. Martinac. 2016. Removal of the mechanoprotective influence of the cytoskeleton reveals Piezo1 is gated by bilayer tension. *Nat. Commun.* 7:10366. <https://doi.org/10.1038/ncomms10366>

Cox, C.D., and P.A. Gottlieb. 2019. Amphipathic molecules modulate Piezo1 activity. *Biochem. Soc. Trans.* 47:1833–1842. <https://doi.org/10.1042/BST20190372>

de Jong, D.H., G. Singh, W.F.D. Bennett, C. Arnarez, T.A. Wassenaar, L.V. Schäfer, X. Periole, D.P. Tieleman, and S.J. Marrink. 2013. Improved parameters for the Martini coarse-grained protein force field. *J. Chem. Theor. Comput.* 9:687–697. <https://doi.org/10.1021/ct300646g>

Deleu, M., J.-M. Crowet, M.N. Nasir, and L. Lins. 2014. Complementary biophysical tools to investigate lipid specificity in the interaction between bioactive molecules and the plasma membrane: A review. *Biochim. Biophys. Acta.* 1838:3171–3190. <https://doi.org/10.1016/j.bbame.2014.08.023>

Dickson, E.J., and B. Hille. 2019. Understanding phosphoinositides: Rare, dynamic, and essential membrane phospholipids. *Biochem. J.* 476:1–23. <https://doi.org/10.1042/BCJ20180022>

Dubin, A.E., M. Schmidt, J. Mathur, M.J. Petrus, B. Xiao, B. Coste, and A. Patapoutian. 2012. Inflammatory signals enhance piezo2-mediated mechanosensitive currents. *Cell Rep.* 2:511–517. <https://doi.org/10.1016/j.celrep.2012.07.014>

Eijkelkamp, N., J.E. Linley, J.M. Torres, L. Bee, A.H. Dickenson, M. Gringhuis, M.S. Minett, G.S. Hong, E. Lee, U. Oh, et al. 2013. A role for Piezo2 in EPAC1-dependent mechanical allodynia. *Nat. Commun.* 4:1682. <https://doi.org/10.1038/ncomms2673>

Fotiou, E., S. Martin-Almedina, M.A. Simpson, S. Lin, K. Gordon, G. Brice, G. Atton, I. Jeffery, D.C. Rees, C. Mignot, et al. 2015. Novel mutations in Piezo1 cause an autosomal recessive generalized lymphatic dysplasia with non-immune hydrops fetalis. *Nat. Commun.* 6:8085. <https://doi.org/10.1038/ncomms9085>

Gimpl, G., K. Burger, and F. Fahrenholz. 1997. Cholesterol as modulator of receptor function. *Biochemistry.* 36:10959–10974. <https://doi.org/10.1021/bi963138w>

- Glogowska, E., E.R. Schneider, Y. Maksimova, V.P. Schulz, K. Lezon-Geyda, J. Wu, K. Radhakrishnan, S.B. Keel, D. Mahoney, A.M. Freidmann, et al. 2017. Novel mechanisms of Piezo1 dysfunction in hereditary xerocytosis. *Blood*. 130:1845–1856. <https://doi.org/10.1182/blood-2017-05-786004>
- Gottlieb, P.A., and F. Sachs. 2012. Piezo1: Properties of a cation selective mechanical channel. *Channels*. 6:214–219. <https://doi.org/10.4161/chan.21050>
- Han, X., and R.W. Gross. 1994. Electrospray ionization mass spectroscopic analysis of human erythrocyte plasma membrane phospholipids. *Proc. Natl. Acad. Sci. USA*. 91:10635–10639. <https://doi.org/10.1073/pnas.91.22.10635>
- Harris, E., A. Topf, R. Barresi, J. Hudson, H. Powell, J. Tellez, D. Hicks, A. Porter, M. Bertoli, T. Evangelista, C. Marini-Betollo, Ó. Magnússon, M. Lek, D. MacArthur, K. Bushby, H. Lochmüller, and V. Straub. 2017. Exome sequences versus sequential gene testing in the UK highly specialised Service for Limb Girdle Muscular Dystrophy. *Orphanet J Rare Dis*. 12:151. <https://doi.org/10.1186/s13023-017-0699-9>
- Hulce, J.J., A.B. Cognetta, M.J. Niphakis, S.E. Tully, and B.F. Cravatt. 2013. Proteome-wide mapping of cholesterol-interacting proteins in mammalian cells. *Nat. Methods*. 10:259–264. <https://doi.org/10.1038/nmeth.2368>
- Humphrey, W., A. Dalke, and K. Schulten. 1996. VMD: Visual molecular dynamics. *J. Mol. Graph.* 14:33–38, 27–28. [https://doi.org/10.1016/0263-7855\(96\)00018-5](https://doi.org/10.1016/0263-7855(96)00018-5)
- Ingólfsson, H.I., M.N. Melo, F.J. van Eerden, C. Arnarez, C.A. Lopez, T.A. Wassenaar, X. Periole, A.H. de Vries, D.P. Tieleman, and S.J. Marrink. 2014. Lipid organization of the plasma membrane. *J. Am. Chem. Soc.* 136:14554–14559. <https://doi.org/10.1021/ja507832e>
- Jiang, W., J.S. Del Rosario, W. Botello-Smith, S. Zhao, Y.-c. Lin, H. Zhang, J. Lacroix, T. Rohacs, and Y.L. Luo. 2021. Crowding-induced opening of the mechanosensitive Piezo1 channel in silico. *Commun. Biol.* 4:84. <https://doi.org/10.1038/s42003-020-01600-1>
- Lai, A., C.D. Cox, N. Chandra Sekar, P. Thurgood, A. Jaworowski, K. Peter, and S. Baratchi. 2022. Mechanosensing by Piezo1 and its implications for physiology and various pathologies. *Biol. Rev. Camb. Philos. Soc.* 97:604–614. <https://doi.org/10.1111/brv.12814>
- Li, J., B. Hou, S. Tumova, K. Muraki, A. Bruns, M.J. Ludlow, A. Sedo, A.J. Hyman, L. McKeown, R.S. Young, et al. 2014. Piezo1 integration of vascular architecture with physiological force. *Nature*. 515:279–282. <https://doi.org/10.1038/nature13701>
- Li, S., Y. You, J. Gao, B. Mao, Y. Cao, X. Zhao, and X. Zhang. 2018. Novel mutations in TPM2 and PIEZO2 are responsible for distal arthrogryposis (DA) 2B and mild DA in two Chinese families. *BMC Medical Genetics*. 19:179. <https://doi.org/10.1186/s12881-018-0692-8>
- Lin, Y.-C., Y.R. Guo, A. Miyagi, J. Levring, R. MacKinnon, and S. Scheuring. 2019. Force-induced conformational changes in Piezo1. *Nature*. 573:230–234. <https://doi.org/10.1038/s41586-019-1499-2>
- Ma, S., S. Cahalan, G. LaMonte, N.D. Grubaugh, W. Zeng, S.E. Murthy, E. Paytas, R. Gamini, V. Lukacs, T. Whitwam, et al. 2018. Common Piezo1 allele in african populations causes RBC dehydration and attenuates plasmodium infection. *Cell*. 173:443–455.e12. <https://doi.org/10.1016/j.cell.2018.02.047>
- Marrink, S.J., H.J. Risselada, S. Yefimov, D.P. Tieleman, and A.H. de Vries. 2007. The MARTINI force field: Coarse grained model for biomolecular simulations. *J. Phys. Chem. B*. 111:7812–7824. <https://doi.org/10.1021/jp071097f>
- McMillin, M.J., A.E. Beck, J.X. Chong, K.M. Shively, K.J. Buckingham, H.I.S. Gildersleeve, M.I. Aracena, A.S. Aylsworth, P. Bitoun, J.C. Carey, et al. 2014. Mutations in Piezo2 cause Gordon syndrome, Marden-Walker syndrome, and distal arthrogryposis type 5. *Am. J. Human Genet.* 94:734–744. <https://doi.org/10.1016/j.ajhg.2014.03.015>
- Mitchell, D.C., M. Straume, J.L. Miller, and B.J. Litman. 1990. Modulation of metarhodopsin formation by cholesterol-induced ordering of bilayer lipids. *Biochemistry*. 29:9143–9149. <https://doi.org/10.1021/bi00491a007>
- Montenegro, F.A., J.R. Cantero, and N.P. Barrera. 2017. Combining mass spectrometry and X-ray crystallography for analyzing native-like membrane protein lipid complexes. *Front. Physiol.* 8:892. <https://doi.org/10.3389/fphys.2017.00892>
- Moroni, M., M.R. Servin-Vences, R. Fleischer, O. Sánchez-Carranza, and G.R. Lewin. 2018. Voltage gating of mechanosensitive Piezo channels. *Nat. Commun.* 9:1096. <https://doi.org/10.1038/s41467-018-03502-7>
- Murthy, S.E., M.C. Loud, I. Daou, K.L. Marshall, F. Schwaller, J. Kühnemund, A.G. Francisco, W.T. Keenan, A.E. Dubin, G.R. Lewin, and A. Patapoutian. 2018. The mechanosensitive ion channel Piezo2 mediates sensitivity to mechanical pain in mice. *Sci. Translat. Med.* 10:eaat9897. <https://doi.org/10.1126/scitranslmed.aat9897>
- Narayanan, P., M. Hütte, G. Kudryasheva, F.J. Taberner, S.G. Lechner, F. Rehfeldt, D. Gomez-Varela, and M. Schmidt. 2018. Myotubularin related protein-2 and its phospholipid substrate PIP2 control Piezo2-mediated mechanotransduction in peripheral sensory neurons. *Elife*. 7:e32346. <https://doi.org/10.7554/eLife.32346>
- Nguetse, C.N., N. Purington, E.R. Ebel, B. Shakya, M. Tetard, P.G. Kremsner, T.P. Velavan, and E.S. Egan. 2020. A common polymorphism in the mechanosensitive ion channel Piezo1 is associated with protection from severe malaria in humans. *Proc. Natl. Acad. Sci. USA*. 117:9074–9081. <https://doi.org/10.1073/pnas.1919843117>
- Okubo, M., A. Fujita, Y. Saito, H. Komaki, A. Ishiyama, E. Takeshita, E. Kojima, R. Koichihara, T. Saito, E. Nakagawa, et al. 2015. A family of distal arthrogryposis type 5 due to a novel Piezo2 mutation. *Am. J. Med. Genet. A*. 167A:1100–1106. <https://doi.org/10.1002/ajmg.a.36881>
- Periole, X., M. Cavalli, S.-J. Marrink, and M.A. Ceruso. 2009. Combining an elastic network with a coarse-grained molecular force field: Structure, dynamics, and intermolecular recognition. *J. Chem. Theor. Comput.* 5:2531–2543. <https://doi.org/10.1021/ct9002114>
- Qi, Y., L. Andolfi, F. Frattini, F. Mayer, M. Lazzarino, and J. Hu. 2015a. Membrane stiffening by STOML3 facilitates mechanosensation in sensory neurons. *Nat. Commun.* 6:8512. <https://doi.org/10.1038/ncomms9512>
- Qi, Y., H.I. Ingólfsson, X. Cheng, J. Lee, S.J. Marrink, and W. Im. 2015b. CHARMM-GUI Martini maker for coarse-grained simulations with the Martini force field. *J. Chem. Theor. Comput.* 11:4486–4494. <https://doi.org/10.1021/acs.jctc.5b00513>
- Ranade, S.S., Z. Qiu, S.-H. Woo, S.S. Hur, S.E. Murthy, S.M. Cahalan, J. Xu, J. Mathur, M. Bandell, B. Coste, et al. 2014a. Piezo1, a mechanically activated ion channel, is required for vascular development in mice. *Proc. Natl. Acad. Sci. USA*. 111:10347–10352. <https://doi.org/10.1073/pnas.1409233111>
- Ranade, S.S., S.-H. Woo, A.E. Dubin, R.A. Moshourab, C. Wetzel, M. Petrus, J. Mathur, V. Bégay, B. Coste, J. Mainquist, et al. 2014b. Piezo2 is the major transducer of mechanical forces for touch sensation in mice. *Nature*. 516:121–125. <https://doi.org/10.1038/nature13980>
- Ridone, P., E. Pandzic, M. Vassalli, C.D. Cox, A. Macmillan, P.A. Gottlieb, and B. Martinac. 2020. Disruption of membrane cholesterol organization impairs the activity of Piezo1 channel clusters. *J. Gen. Physiol.* 152:e201912515. <https://doi.org/10.1085/jgp.201912515>
- Romero, L.O., R. Caires, A.R. Nickolls, A.T. Chesler, J.F. Cordero-Morales, and V. Vásquez. 2020. A dietary fatty acid counteracts neuronal mechanical sensitization. *Nat. Commun.* 11:2997. <https://doi.org/10.1038/s41467-020-16816-2>
- Romero, L.O., A.E. Massey, A.D. Mata-Daboin, F.J. Sierra-Valdez, S.C. Chauhan, J.F. Cordero-Morales, and V. Vásquez. 2019. Dietary fatty acids fine-tune Piezo1 mechanical response. *Nat. Commun.* 10:1200. <https://doi.org/10.1038/s41467-019-09055-7>
- Sampaio, J.L., M.J. Gerl, C. Klose, C.S. Ejsing, H. Beug, K. Simons, and A. Shevchenko. 2011. Membrane lipidome of an epithelial cell line. *Proc. Natl. Acad. Sci. USA*. 108:1903–1907. <https://doi.org/10.1073/pnas.1019267108>
- Shi, J., A.J. Hyman, D. De Vecchis, J. Chong, L. Lichtenstein, T.S. Futers, M. Rouahi, A.N. Salvayre, N. Auge, A.C. Kalli, and D.J. Beech. 2020. Sphingomyelinase disables inactivation in endogenous Piezo1 channels. *Cell Rep*. 33:108225. <https://doi.org/10.1016/j.celrep.2020.108225>
- Shin, K.C., H.J. Park, J.G. Kim, I.H. Lee, H. Cho, C. Park, T.S. Sung, S.D. Koh, S.W. Park, and Y.M. Bae. 2019. The Piezo2 ion channel is mechanically activated by low-threshold positive pressure. *Sci. Rep.* 9:6446. <https://doi.org/10.1038/s41598-019-42492-4>
- Syeda, R., M.N. Florendo, C.D. Cox, J.M. Kefauver, J.S. Santos, B. Martinac, and A. Patapoutian. 2016. Piezo1 channels are inherently mechanosensitive. *Cell Rep*. 17:1739–1746. <https://doi.org/10.1016/j.celrep.2016.10.033>
- Szczot, M., J. Liljencrantz, N. Ghitani, A. Barik, R. Lam, J.H. Thompson, D. Bharucha-Goebel, D. Saade, A. Nécaise, S. Donkersvoort, et al. 2018. Piezo2 mediates injury-induced tactile pain in mice and humans. *Sci. Translat. Med.* 10:eaat9892. <https://doi.org/10.1126/scitranslmed.aat9892>
- Van Der Spoel, D., E. Lindahl, B. Hess, G. Groenhof, A.E. Mark, and H.J.C. Berendsen. 2005. GROMACS: Fast, flexible, and free. *J. Comput. Chem.* 26:1701–1718. <https://doi.org/10.1002/jcc.20291>
- Virtanen, J.A., K.H. Cheng, and P. Somerharju. 1998. Phospholipid composition of the mammalian red cell membrane can be rationalized by a superlattice model. *Proc. Natl. Acad. Sci. USA*. 95:4964–4969. <https://doi.org/10.1073/pnas.95.9.4964>

- Wang, L., H. Zhou, M. Zhang, W. Liu, T. Deng, Q. Zhao, Y. Li, J. Lei, X. Li, and B. Xiao. 2019. Structure and mechanogating of the mammalian tactile channel Piezo2. *Nature*. 573:225–229. <https://doi.org/10.1038/s41586-019-1505-8>
- Wassenaar, T.A., H.I. Ingólfsson, R.A. Böckmann, D.P. Tieleman, and S.J. Marrink. 2015. Computational lipidomics with insane: A versatile tool for generating custom membranes for molecular simulations. *J. Chem. Theor. Comput.* 11:2144–2155. <https://doi.org/10.1021/acs.jctc.5b00209>
- Woo, S.-H., V. Lukacs, J.C. de Nooij, D. Zaytseva, C.R. Criddle, A. Francisco, T.M. Jessell, K.A. Wilkinson, and A. Patapoutian. 2015. Piezo2 is the principal mechanotransduction channel for proprioception. *Nature Neurosci.* 18:1756–1762. <https://doi.org/10.1038/nn.4162>
- Zeng, W.-Z., K.L. Marshall, S. Min, I. Daou, M.W. Chapleau, F.M. Abboud, S.D. Liberles, and A. Patapoutian. 2018. PIEZO2 mediates neuronal sensing of blood pressure and the baroreceptor reflex. *Science*. 362:464–467. <https://doi.org/10.1126/science.aau6324>
- Zhang, M., Y. Wang, J. Geng, S. Zhou, and B. Xiao. 2019. Mechanically activated Piezo channels mediate touch and suppress acute mechanical pain response in mice. *Cell Rep.* 26:1419–1431.e4. <https://doi.org/10.1016/j.celrep.2019.01.056>
- Zhao, Q., H. Zhou, S. Chi, Y. Wang, J. Wang, J. Geng, K. Wu, W. Liu, T. Zhang, M.-Q. Dong, J. Wang, X. Li, and B. Xiao. 2018. Structure and mechanogating mechanism of the Piezo1 channel. *Nature*. 554:487–492. <https://doi.org/10.1038/nature25743>
- Zheng, W., Y.A. Nikolaev, E.O. Gracheva, and S.N. Bagriantsev. 2019. Piezo2 integrates mechanical and thermal cues in vertebrate mechanoreceptors. *Proc. Natl. Acad. Sci. USA*. 116:17547–17555. <https://doi.org/10.1073/pnas.1910213116>

## Supplemental material

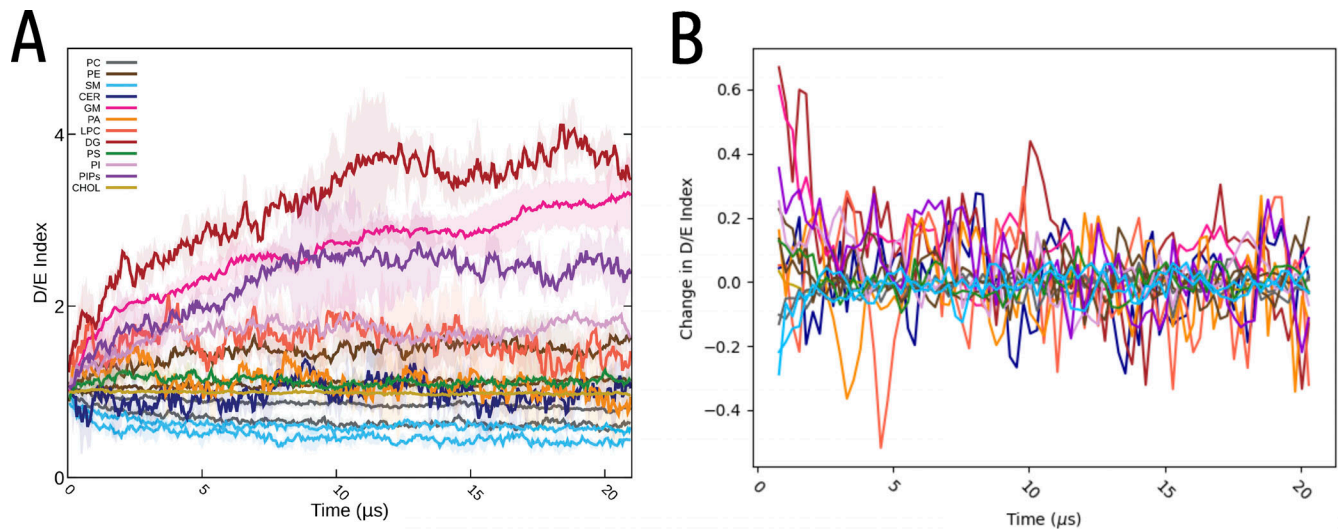


Figure S1. **Lipid D/E index over time to assess convergence.** (A) The lipid D/E was calculated every 50 ns and graphed over time. SDs are calculated between replicates and represented using pale bands around each line. For some lipids (PC, PE, and SM), there are two lines, one corresponding to the upper leaflet value, and one corresponding to the lower leaflet value. It was determined that the D/E index converged after 14  $\mu$ s. (B) Changes in lipid D/E index over time calculated in 250-ns blocks and shown as a rolling average to reduce noise.

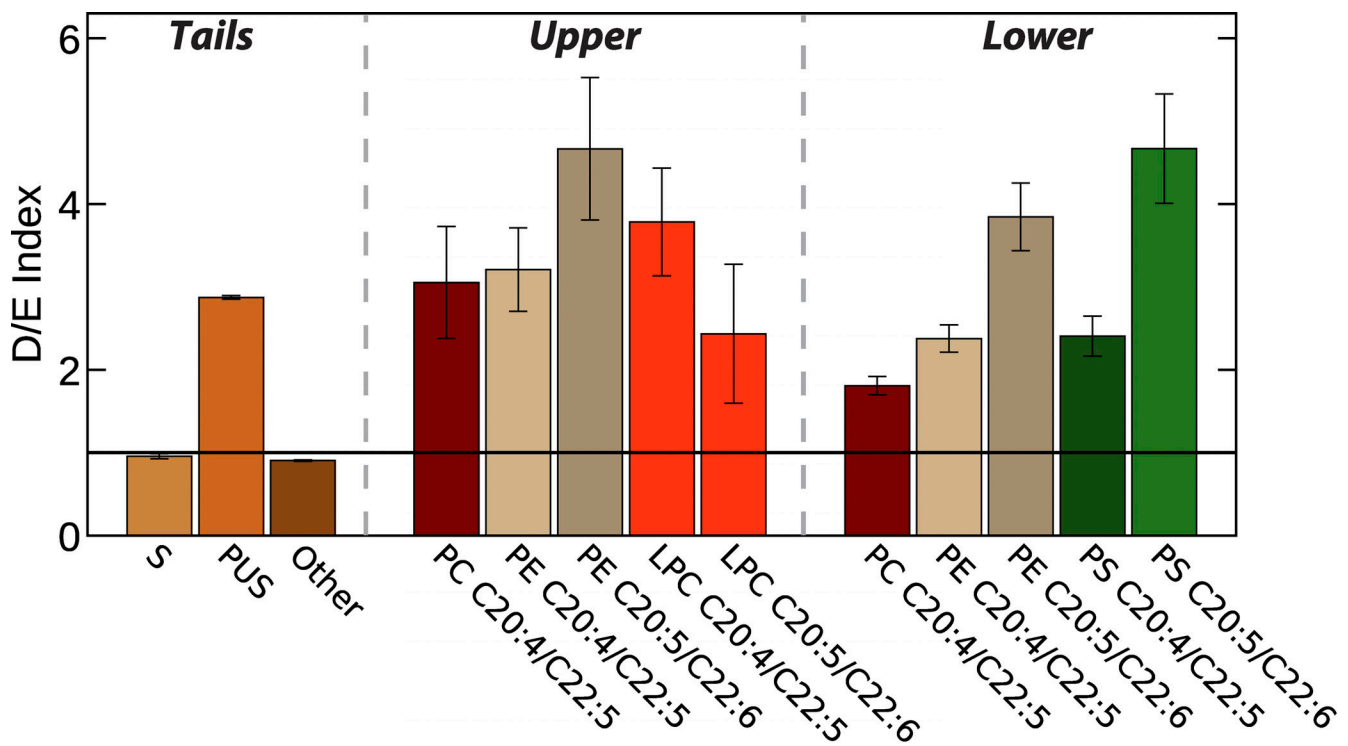


Figure S2. **Lipid D/E index of the PUS fatty acids (PUFAs) in the system, averaged between three replicates and including SD.** Two types of lipid tails are listed under the bar graph, as the CG lipid can represent either of these two tails. S, saturated.

PC PE SM CER GM PA DG PS PI PIP CHOL

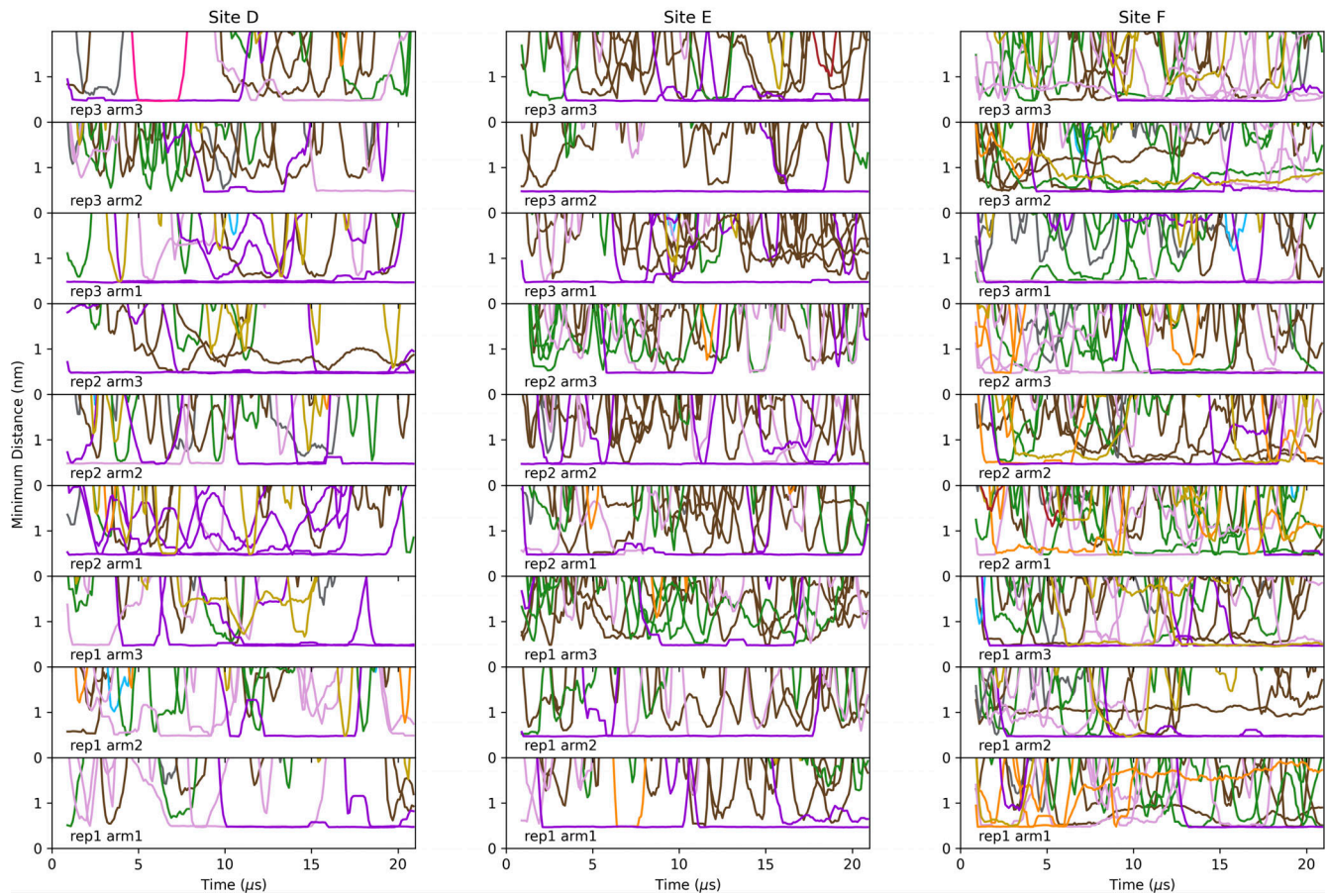


Figure S3. Minimum distance between contacting lipids and PIP binding sites D (left), E (middle), and F (right) on each arm of Piezo2 across each replicate plotted over simulation time. Note that analysis was performed on the last 7  $\mu\text{s}$  only (14–21  $\mu\text{s}$ ) to ensure the system was equilibrated.

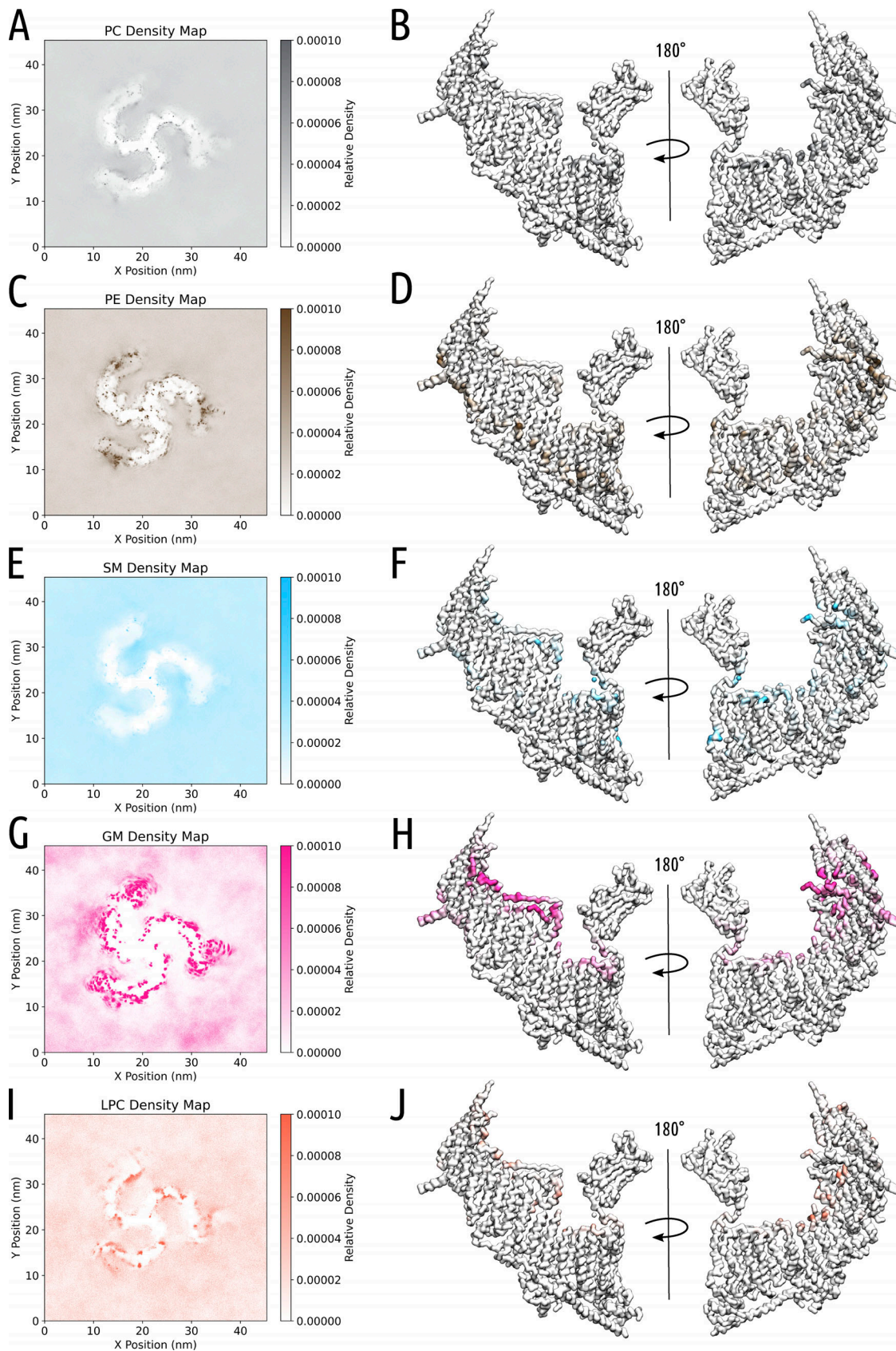


Figure S4. **Density maps and occupancy surfaces for other lipids.** (A–J) Density maps and contacts on the Piezo2 structure for PC (A and B), PE (C and D), SM (E and F), glycolipids (G and H), and LPC (I and J). The structure of Piezo2 is represented as surface, with the contacts mapped as a percentage: the darker the color, the higher the occupancy the lipid has with Piezo2 throughout the last 7  $\mu$ s of simulation time.

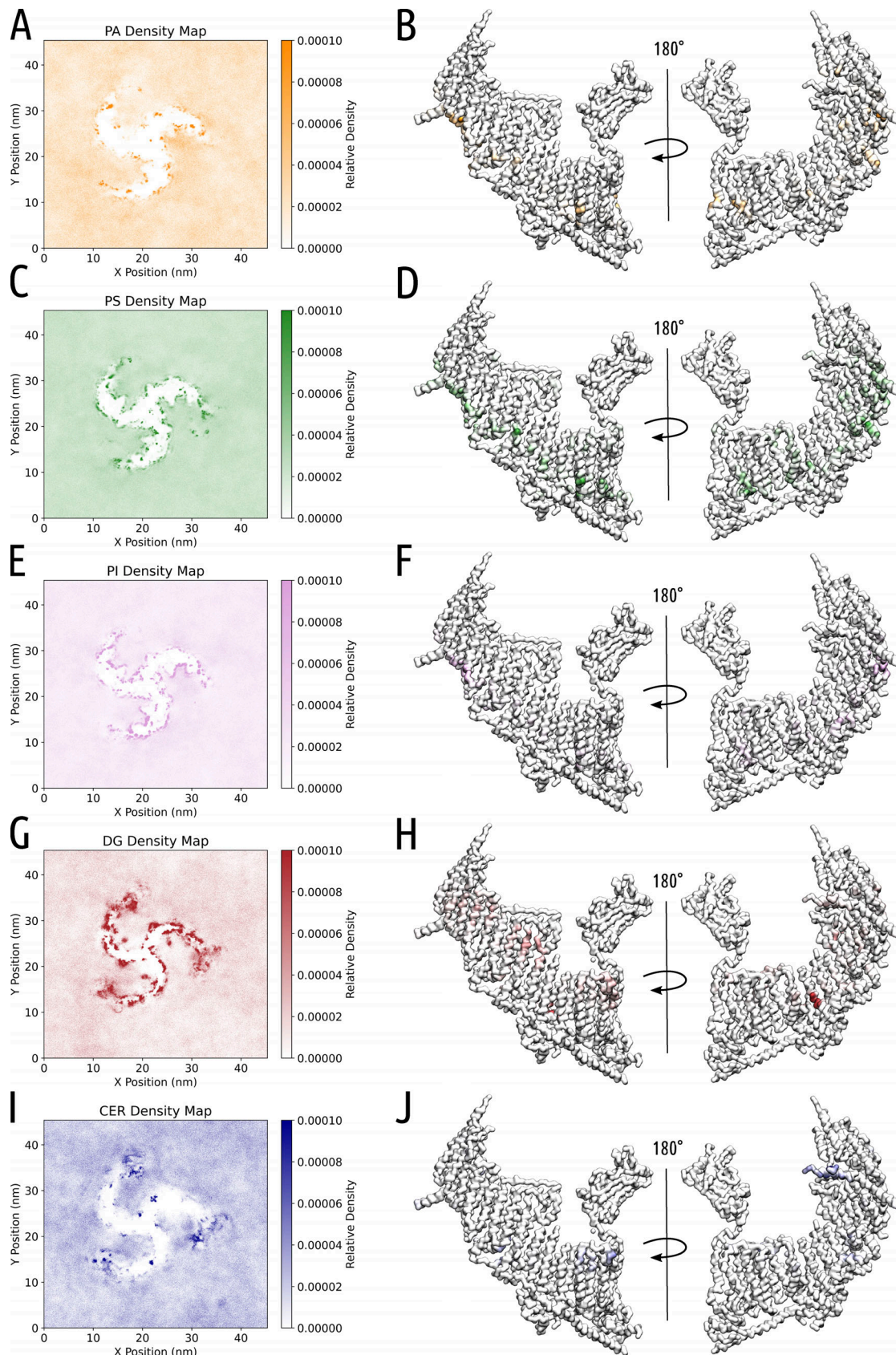


Figure S5. **Density maps and occupancy surfaces for other lipids.** (A–J) Density maps and contacts on the Piezo2 structure for PA (A and B), PS (C and D), PI (E and F), DG (G and H), and CER (I and J). The structure of Piezo2 is represented as surface, with the contacts mapped as a percentage: the darker the color, the higher the occupancy the lipid has with Piezo2 throughout the last 7  $\mu$ s of simulation time.



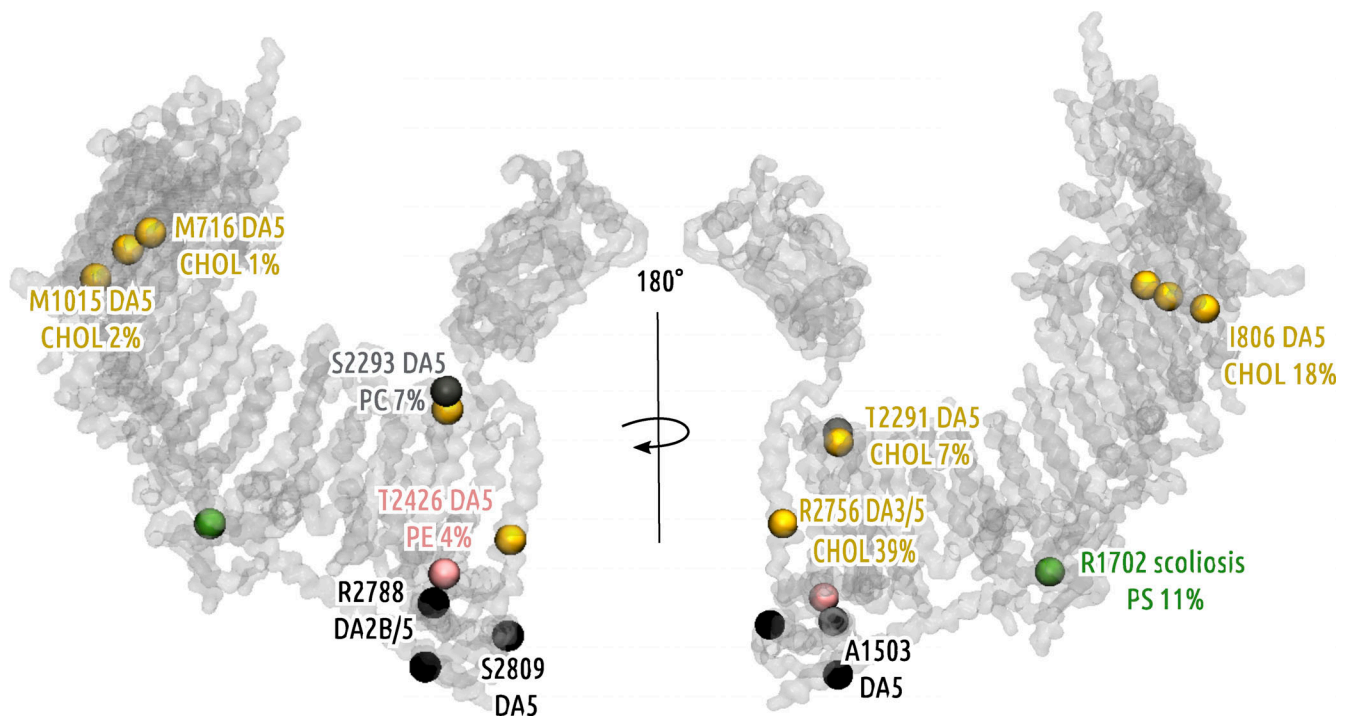


Figure S6. **Locations of disease-causing mutations.** Each mutation is represented on the Piezo2 structure by spheres. Black residues do not interact with a lipid headgroup. Other residues are colored by the main lipid that they interact with. The protein backbone is represented in silver glass. Diseases associated with each mutation are noted (DA5, distal arthrogyrosis type 5; DA3, distal arthrogyrosis type 3; DA2B, distal arthrogyrosis type 2B).

Provided online are Table S1, Table S2, and Table S3. Table S1 contains information on the Piezo2 model used in our simulations. Table S2 shows lipid composition of Piezo2 simulations. Table S3 shows lipid interactions at disease-causing mutations.